Journal of Computational Physics 351 (2017) 358–375

Contents lists available at ScienceDirect

Journal of Computational Physics

www.elsevier.com/locate/jcp

# Kinetic simulation technique for plasma flow in strong external magnetic field

Frans H. Ebersohn [a,*], J.P. Sheehan [a], Alec D. Gallimore [a], John V. Shebalin [b]

[a] University of Michigan, Ann Arbor, MI, 48109, USA
[b] NASA Johnson Space Center, Exploration Integration and Science Directorate, Houston, TX, 77058, USA

ARTICLE INFO

*Article history:*
Received 6 February 2017
Received in revised form 31 July 2017
Accepted 9 September 2017

*Keywords:*
Quasi-one-dimensional
Magnetized
Plasma
Simulation
Modeling
Particle-in-cell
Kinetic
Flux tube
Magnetic mirror

ABSTRACT

A technique for the kinetic simulation of plasma flow in strong external magnetic fields was developed which captures the compression and expansion of plasma bound to a magnetic flux tube as well as forces on magnetized particles within the flux tube. This quasi-one-dimensional (Q1D) method resolves a single spatial dimension while modeling two-dimensional effects. The implementation of this method in a Particle-In-Cell (PIC) code was verified with newly formulated test cases which include two-particle motion and particle dynamics in a magnetic mirror. Results from the Q1D method and fully two dimensional simulations were compared and error analyses performed verifying that the Q1D model reproduces the fully 2D results in the correct regimes. The Q1D method was found to be valid when the hybrid Larmor radius was less than 10% of the magnetic field scale length for magnetic field guided plasma expansions and less than 1% of the magnetic field scale length for a plasma in a converging–diverging magnetic field. The simple and general Q1D method can readily be incorporated in standard 1D PIC codes to capture multi-dimensional effects for plasma flow along magnetic fields in parameter spaces currently inaccessible by fully kinetic methods.



## 1. Introduction

Plasma expansion guided by a strong external magnetic field is prevalent in both nature and the laboratory. Space plasmas in particular have many examples of magnetized plasmas [1–3]. In the laboratory, magnetized plasma jet expansions are an integral part of plasma sources used for spacecraft propulsion [4–7] and plasma processing [8–12]. In spacecraft propulsion, the strong magnetic field guiding the plasma flow is known as a magnetic nozzle which is used to generate thrust by accelerating plasma generated by a source into a directed beam [13–16]. Random thermal energy in the plasma is converted into directed kinetic energy in the converging–diverging (or just diverging) magnetic field of the magnetic nozzle.

The physics of magnetic field guided plasma expansion includes non-equilibrium and multidimensional effects. The plasma guided by the magnetic field can originate from a thermal or non-thermal source region [17]. As the plasma expands, collisions become infrequent and non-equilibrium effects become increasingly important. The presence of non-equilibrium effects requires that a kinetic description be used to describe the plasma dynamics. The presence of the magnetic field also introduces inherent multidimensional effects due to the magnetic field forces and expansion of the plasma along the magnetic field. Overall, theoretical treatment of this non-equilibrium, multidimensional problem is non-trivial and numerical simulations become essential for studying the fundamental physics.

* Corresponding author.
*E-mail address:* ebersohn@umich.edu (F.H. Ebersohn).

http://dx.doi.org/10.1016/j.jcp.2017.09.021
0021-9991/

Numerical simulation of expanding plasma jets is expensive due to the physical regimes modeled and the multidimensionality of the problem. Simplifications have been made by studying the problem with multidimensional fluid models which assume equilibrium plasma behavior, neglecting kinetic effects [18–21]. Conversely, kinetic methods have been used which simulate one dimension [22,23] or truncate simulation domains [24,25].

This paper introduces a novel technique for simulating magnetic field guided plasma flows and was developed to address the current challenges with numerically modeling these plasmas. The method includes multidimensional effects without the costs associated with full multidimensional simulations. The magnetized plasma problem was reduced to a single spatial dimension by assuming that the particles are magnetized and bound to a magnetic field line. This method models the flow of plasma along a magnetic flux-tube, spatially resolving the magnetic field direction while accounting for the multidimensional effects of the changing magnetic field such as the compression and expansion of the plasma. The model includes a particle mover for the magnetized particles and cross-sectional area variation for the quasi-one-dimensional cells along the magnetic field direction. The method was incorporated in a one dimensional Particle-In-Cell (PIC) scheme [26–28] which was verified through simple test cases and comparison with fully two dimensional simulations.

The new method builds on previous work, [29,30] but is novel in its generality, the physics captured, and scope of application. Similar particle movers have been developed by Vu et al. [30] and Vedin et al. [29]. The work of Vu et al. included a force using the magnetic moment to correct errors in cross field particle drifts for large time steps (greater than the cyclotron period). This was a different application than presented in this paper which instead solved for motion along a magnetic field. Vedin et al.'s work modeled the flow of plasma along auroral flux tubes, an application very similar to that presented in this work. However, their method used a hybrid approach with was a mixture of kinetic and continuum methods. The particle mover used assumed a constant magnetic moment which limits the application of this model to collisionless plasmas. Furthermore, Vedin et al. included a correction directly to the electric field to keep density and current consistent with the fluid equations. Their method was significantly different from the area variation presented here.

The work presented herein expands on Vu et al. and Vedin et al.'s work by adding a more general formulation for particle motion along a magnetic field line. The new method does not explicitly assume a constant magnetic moment, enabling its application to other problems such as collisional plasmas. The method can be used to study the fully kinetic flow of plasma along a magnetic flux tube for a fraction of the computational cost of the current alternative of higher dimensional simulations.

The theory behind the model is presented in Section 2. Section 3 introduces the new, quasi-one-dimensional (Q1D) method and discusses the implementation of this method into a one dimensional PIC code. Section 4 presents verification of the Q1D method with two newly formulated test problems. Section 5 presents further verification by comparing the Q1D simulation results with fully two dimensional simulation results. Section 6 discusses the results of the verification simulations and Section 7 concludes the paper.

## 2. Theory

### 2.1. Particle description

Particle motion in electric and magnetic fields is governed by the Lorentz force (**F**) shown below:

$$\mathbf{F} = m\frac{d\mathbf{v}}{dt} = q(\mathbf{E} + \mathbf{v} \times \mathbf{B}) \tag{1}$$

In this equation **v** is the velocity, **E** the electric field, **B** the magnetic field, and q the particle charge. This force can be simplified by assuming that the particles are bound to a magnetic field line and then adopting a cylindrical coordinate system along the magnetic field line. In the new, cylindrical coordinate system inertial forces ($\mathbf{F_I}$) must also be included as shown below.

$$m\frac{d\mathbf{v}}{dt} = q(E + \mathbf{v} \times \mathbf{B}) + \mathbf{F}_i \tag{2}$$

$$\mathbf{F}_i = m\frac{v_\theta^2}{r}\hat{r} - m\frac{v_\theta v_r}{r}\hat{\theta}. \tag{3}$$

Magnetically bound particles are displaced from the magnetic field by their Larmor radii ($r_L$) and it was assumed that there is negligible variation of the axial magnetic field over the particle orbit. Combined with Gauss' Law of Magnetism, this leads to an expression for an average radial magnetic field over the particle orbit ($B_r$).

$$B_r = -\frac{r_L}{2}\frac{dB_z}{dz} \tag{4}$$

In this equation $r_L = \frac{mv_\theta}{qB}$ in which $v_\theta$ is the azimuthal velocity perpendicular to the magnetic field and $m$ is the mass of the particle. The assumptions made in this derivation are very similar to those made in examining magnetic mirror physics [31].

Substituting Equation (4) into Equation (2) while using the Larmor radius as $r$ (and temporarily ignoring the electric field) leads to a significant simplification as the inertial forces cancel some of the magnetic field forces. Physically, this cancellation

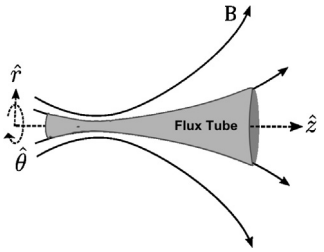


**Fig. 1.** Flux-tube used for calculating cross sectional area variation.

occurs due to the assumption of magnetization of the particles. The magnetic field forces confine the particles to following the axis, which is a magnetic field line. The remaining terms are shown below in Equations (5)–(7) and represent the magnetic dipole force on a magnetized particle as well as the kinetic energy conserving force.

$$m\frac{dv_z}{dt} = -\frac{m}{2B_z}\frac{dB_z}{dz}v_\theta^2 \tag{5}$$

$$m\frac{dv_\theta}{dt} = \frac{m}{2B_z}\frac{dB_z}{dz}v_\theta v_z \tag{6}$$

$$m\frac{dv_r}{dt} = 0 \tag{7}$$

Implicit in this derivation is the assumption of changing to a frame of reference along the field line where the azimuthal velocity ($v_\theta$) is the velocity perpendicular to the field line ($v_\perp$). The perpendicular velocity defines the particle orbit. The velocity was reduced to two dimensions, one along the magnetic field line and one perpendicular to the magnetic field line. These simplified equations (now including the electric field) are shown below in which $s$ is the direction along the magnetic field line:

$$m\frac{dv_\parallel}{dt} = qE_\parallel - \frac{m}{2B}\frac{dB}{ds}v_\perp^2 \tag{8}$$

$$m\frac{dv_\perp}{dt} = qE_\perp + \frac{m}{2B}\frac{dB}{ds}v_\perp v_\parallel \tag{9}$$

The parallel force is the magnetic mirror force which accelerates particles from high to low magnetic field regions, while the perpendicular force ensures energy conservation.

### 2.2. Continuum description

Substituting the equations derived above into the Vlasov–Boltzmann equation and integrating leads to the following continuum equations for mass and axial momentum conservation [2,17]:

$$\frac{\partial n}{\partial t} + \nabla\cdot(n\mathbf{u}) = 0 \tag{10}$$

$$nm\frac{D\mathbf{u}_\parallel}{Dt} = nq(\mathbf{E}_\parallel) - \nabla_\parallel p_\parallel + \left(\frac{p_\parallel - p_\perp}{B}\right)\nabla_\parallel B \tag{11}$$

In these equations $n$ is the number density, $u$ is the mean velocity, $p$ is the pressure, $q$ is the charge, and $m$ is the mass.

This description includes non-equilibrium effects such as anisotropic temperatures. Furthermore, it captures the effects of the magnetic mirror force on the continuum level by including the anisotropic pressure force term in Equation (11) [17,32].

#### 2.2.1. Quasi-one-dimensional description

Assuming particles are confined to magnetic field lines implies that particles are trapped within a magnetic flux tube such that shown in Fig. 1. Integrating Gauss' law of magnetization and assuming radial contributions to the flux are negligible leads to the following expression in which $A$ is the cross sectional area of the flux tube and hence the plasma:

$$BA = constant \tag{12}$$

This expression can be used to further simplify the physical description of the plasma by constraining the plasma volume to the known area of the magnetic flux tube and assuming that the plasma properties are constant across the flux tube cross-section. This treatment results in a quasi-one-dimensional description of the plasma where the plasma properties vary along a magnetic field line and the plasma is constrained to a certain volume by a magnetic wall. An example of the resulting steady state, integrated, continuity equation is shown below:

$$\frac{nu}{B} = constant \tag{13}$$

## 3. Method

As mentioned in the previous section, the multidimensional plasma dynamics can be simplified by assuming that the plasma is bound to a magnetic flux tube with plasma properties which are constant across the flux-tube. Additionally, a simplified Lorentz force which mimics the magnetic mirror force was found. These simplifications rely on two fundamental assumptions: (1) Forces due to the magnetic field are strong enough to confine the plasma and cross-field diffusion of the plasma is negligible; and (2) Magnetized particles experience the magnetic mirror force. The computational representation of the physical model presented in the previous section is described in this section.

The Q1D method was implemented as an extension to the standard 1D3V (one spatial dimension, three velocity dimensions) electrostatic particle-in-cell (PIC) method [26–28]. To accommodate the Q1D model the cell areas were non-uniform and the forces due to the changing magnetic field were included.

### 3.1. Area variation

The effects of expansion and compression of the plasma by the magnetic field were included in a 1D PIC scheme by varying the plasma sheet cross-sectional area according to the magnetic field strength. The cross-sectional area at each grid point ($i$) was found by using Equation (14).

$$A_i = \frac{B_0}{B_i} A_0 \tag{14}$$

In this expression $B$ is the magnitude of the magnetic field, $A$ is the area perpendicular to the magnetic field direction, and the subscript 0 refers to a reference point. The area anywhere in the domain can be computed from the cross-sectional area at a single point and the applied magnetic field in the domain. The cell volume, used to calculate continuum properties, was the product of the cell's cross-sectional area and the cell width.

### 3.2. Particle mover

The standard leap-frog algorithm (shown below) was used for the particle mover [26].

$$s^{n+1/2} = s^{n-1/2} + v_\parallel^n \Delta t \tag{15}$$

$$\mathbf{v}^{n+1} = \mathbf{v}^n + \mathbf{a}^{n+1/2} \Delta t \tag{16}$$

In these equations $\Delta t$ is the time step, $s$ is the direction along the magnetic field, $n$ is the index for the time step, and $\mathbf{a}$ the acceleration described by the forces from Equations (8) and (9). The particle position and velocity were offset by half a time step. The acceleration was calculated using properties at the intermediate time step between velocity time steps.

The Lorentz force was applied with method similar to the three step Boris method used in 1D electrostatic PIC codes [33]. An initial half push to the velocity was performed with the electric field which was followed by the magnetic field forces (see Equations (8) and (9)). These forces rotate the velocity vector, similar to that done by Boris. A final half-push by the electric field was applied after the magnetic field force. Analytical expressions were derived to account for the magnetic mirror force effects on the particle motion according to Equations (8) and (9). Energy conservation during the magnetic field velocity vector rotation requires that the following be true for the steps after the initial electric field push ($-$) and before the final electric field push ($+$):

$$(v_\parallel^-)^2 + (v_\perp^-)^2 = (v_\parallel^+)^2 + (v_\perp^+)^2 = \mathrm{v}^2 \tag{17}$$

Here v is the magnitude of the velocity during the magnetic field push.

An additional equation was found by combining and integrating the equations of motion over the time ($\Delta t$) while assuming that the quantity $\zeta = \frac{1}{2B}\frac{dB}{ds}$ is constant during the time step using properties at step $n+1/2$. The parallel velocity before and after the magnetic field push are:

$$\frac{v_\parallel^+}{\mathrm{v}} = \tanh\left[\operatorname{atanh}\left(\frac{v_\parallel^-}{\mathrm{v}}\right) - \zeta^{n+1/2}\mathrm{v}\Delta t\right] \tag{18}$$

This equation was used to update the parallel velocity due to the magnetic field force. The perpendicular velocity was then updated with the following equation:

$$v_\perp^+ = \sqrt{\mathrm{v}^2 - \left(v_\parallel^+\right)^2} \tag{19}$$

These equations guarantee energy conservation during the magnetic field push and ensure the velocity magnitude is constant. The quantity $\zeta$ was weighted from the nearby grid points and was based on the current position of the particle at the half time step $(n+1/2)$ between the velocity time steps $(n, n+1)$. The quantity $\zeta$ was updated once the particle position changed. Assumption of a constant $\zeta$ during the time step implies that the magnetic field mover is first order accurate in time.

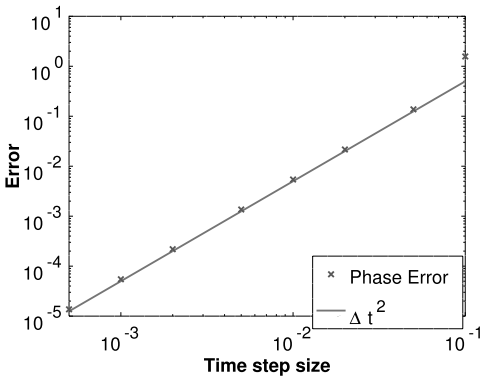


**Fig. 2.** Phase error with time step size for simple harmonic oscillator.

*3.2.1. Error and stability*

The error and stability of the leap-frog algorithm with the new simplified Lorentz force (excluding area variation) was evaluated by considering the problem of a simple harmonic oscillator similar to that done by Birdsall [26]. Treating the magnetic moment ($\mu = mv_{\perp}^2/2B$) as a constant and prescribing a magnetic field of the form $B = Cz^2 + B_0$ (in which C is a constant) resulted in the following equation:

$$\frac{dv_{\parallel}}{dt} = 2C\mu z \tag{20}$$

with a solution:

$$x = D_1 sin(\omega_{osc} t) + D_2 cos(\omega_{osc} t) \tag{21}$$

In this equation $D_1$ and $D_2$ are constants and $\omega_{osc} = \sqrt{2C\mu}$ is the oscillation frequency. Using this result, the error in the phase ($\epsilon$) for the leap frog algorithm was found to be governed by the following equation [26]:

$$\epsilon \propto N(\omega_{osc})\Delta t^3 \tag{22}$$

In this equation $N$ is the number of time steps $\Delta t$. For simulations run out to the same total time ($N\Delta t$) the error goes as $\Delta t^2$. Simulations were performed using the leap frog algorithm with the new magnetic field particle mover and the resulting error in phase is shown in Fig. 2. The phase error scales correctly with the predicted theory.

*3.3. Special considerations*

The Q1D method requires parallel and perpendicular velocities, which need special treatment when incorporated in 1D3V PIC codes in Cartesian space. Three velocity coordinates are essential for treating collisions. To maintain the 1D3V nature, the quasi-1D effects were incorporated by assigning a velocity to be the parallel direction ($\hat{z}$) which was spatially resolved. The other velocities ($\hat{x}, \hat{y}$) were combined to be the perpendicular velocity ($v_{\perp} = \sqrt{v_x^2 + v_y^2}$). Changes in the perpendicular velocity were scaled equally to both the perpendicular directions.

*3.4. PIC code*

Simulations in this paper were performed with the Self-consistent Quasi-1D (SQu1D) code which was developed to study the plasma dynamics of magnetic field guided plasma discharges in electric propulsion devices. The code is a parallelized 1D3V PIC code which includes neutral collisions, plasma heating algorithms, and Coulomb collisions. For the simulations in this paper the following options were used: linear weighting to and from the particles, standard leap-frog algorithm, second order central difference scheme for Poisson's equation, Intel Math Kernel Library LAPACK math libraries for matrix mathematics, and no collision algorithms. Particles were seeded according to standard loading algorithms [34].

## 4. Verification problems

*4.1. Two particle motion*

A simple two-particle verification test was used to compare simulation results to analytical solutions for the motion of two like-charged particles in a magnetic field. The particles begin an initial distance apart with velocities toward one another.

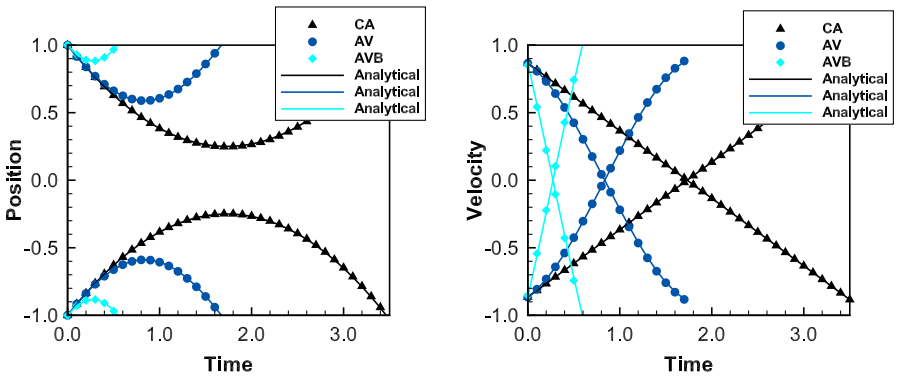


(a) Particle position in time. (b) Particle velocity in time.

**Fig. 3.** Comparison of simulation and analytical results for two-particle motion. Constant area (CA), Area Varying (AV), and Area Varying with magnetic field force (AVB) results are shown.

*4.1.1. Theory*

1D and Q1D PIC codes treat the plasma as sheets of charged particles. When particles flow into regions with a stronger magnetic field, the plasma sheets shrink as the magnetic field compresses the charges and the flux tube area decreases, increasing the charge density. The force on each particle sheet can be re-expressed using the relations for the cross-sectional area in Equation (14).

$$F_z^{\pm} = \left(\frac{Q^2 B^{\pm}}{2B_0 A_0 \epsilon_0}\right) - \frac{m v_{\perp,0}^2}{2B_0} \nabla B^{\pm} \tag{23}$$

Here the $\pm$ superscript refers to the particles starting to the right and left respectively and 0 refers to conditions at the particle origins (which are the same due to symmetry about the origin).

Analytical solutions for the particle motion can be computed when the magnetic field is chosen to be $B = B^* + \alpha^{\pm} z$. This magnetic field is a piecewise continuous function for which $\alpha^{\pm}$ is the constant magnitude slope which is positive ($\alpha^+$) for $z > 0$ and negative ($\alpha^-$) for $z < 0$. The magnetic field strength at $z = 0$ is $B^*$. For simplicity the following parameters were also used: $Q = m = \epsilon_0 = A_0 = 1$. The initial conditions for the particles were set to $z_0^{\pm} = \pm 1$ and $v_0^{\pm} = \mp\sqrt{3}/2$. The initial perpendicular velocity is a free parameter which was also chosen to facilitate simple analytical solutions:

$$v_{\perp,0} = \sqrt{\frac{Q^2 B^*}{\epsilon_0 A_0 m \alpha}} \tag{24}$$

The charge sheet position ($z$) and velocity ($v$) as a function of time using these parameters are:

$$z^{\pm} = \mp\sqrt{\frac{3B_0}{2\alpha}} \sin\left(\sqrt{\frac{\alpha}{2B_0}} t\right) \mp \frac{B_0 + B^*}{\alpha} \cos\left(\sqrt{\frac{\alpha}{2B_0}} t\right) \pm \left(1 + \frac{B_0 + B^*}{\alpha}\right) \tag{25}$$

$$v^{\pm} = \mp\frac{\sqrt{3}}{2} \cos\left(\sqrt{\frac{\alpha}{2B_0}} t\right) \pm \frac{(B_0 + B^*)}{2\sqrt{B_0 \alpha}} \sin\left(\sqrt{\frac{\alpha}{2B_0}} t\right) \tag{26}$$

*4.1.2. Results*

Simulations were performed for several different test cases. The first of these was a 1D constant area simulation (CA) with no Q1D effects included. The second was a test case in which the effects of varying the plasma cross section were included (AV) but not the effects of the Q1D magnetic field forces. Finally a full simulation was performed including the magnetic field forces (AVB). Results shown here were for a grid size of $\Delta z = 0.01$ and time step of $\Delta t = 0.005$.

The analytical solution and the simulation results for the position and velocity of the particles are shown in Fig. 3. In the constant area simulations the particles took the longest time to reflect due the weakest repelling force while simulations including the area variation and magnetic field forces demonstrated the most rapid particle reflection due to the strongest repelling forces. Furthermore, constant area results showed a linear change in the velocity in time due to the constant force applied. The test cases with area variation demonstrated non-linear changes in the velocity over time due to the changing force as the particle sheets are compressed.

The root-mean-square (RMS) errors between the computed and analytical solution are summarized in Table 1. Errors were normalized by the mean velocity or position of the particle during the simulation to get a percent RMS error. The error in each of these cases was small (around 1%) verifying that the method agreed well with the analytically predicted behavior. These results verified the incorporation of the Q1D method in the particle mover and weighting algorithms of a 1D code.

**Table 1**
RMS error for quasi-one-dimensional verification simulations.

| Simulation | Position | Velocity |
|---|---|---|
| Constant area | 0.23% | 0.14% |
| Varying area | 0.091% | 0.20% |
| Varying area and magnetic force | 0.22% | 1.1% |

**Table 2**
Number of trapped particles for magnetic mirror simulations.

| | Simulation | Analytical | Error |
|---|---|---|---|
| Case 1 | 7121 | 7071 | 0.7% |
| Case 2 | 2613 | 2601 | 0.5% |
| Case 3 | 9279 | 9302 | 0.2% |

### 4.2. Magnetic mirror verification

Simulations of particle motion between two magnetic mirrors (regions of increasing magnetic field) were performed to test the Q1D form of the magnetic field Lorentz force. These tests do not solve Poisson's equation and the particles were uncoupled from one another.

#### 4.2.1. Theory

Magnetized particles which move into a region with a stronger magnetic field experience a force which acts from the strong to the weak magnetic field region that can cause particles to be reflected. These regions of increasing magnetic field strength are known as magnetic mirrors. When two magnetic mirrors are placed adjacent one another, particles can be trapped between the two mirrors. An applied electric field can also be incorporated, which increases or decreases the number of particles confined.

The condition for confinement by a magnetic mirror machine, including electric field effects, is:

$$v_{\perp,0} > \sqrt{\frac{v_{\parallel,0}^2 - \frac{2q}{m}\Delta\phi}{R-1}} \tag{27}$$

In this equation $R = \frac{B_{max}}{B_0}$ is the mirror ratio of the magnetic confinement device, $B_{max}$ is the maximum magnetic field, $B_0$ is the initial magnetic field, $v_{\perp,0}$ is the initial perpendicular velocity, $v_{\parallel,0}$ is the initial parallel velocity, and $\Delta\phi$ is the potential drop which occurs between the $B_0$ and $B_{max}$ points. This relationship is used to define the velocity space of the trapped and lost particles.

Integrating the velocity distribution using the constraints of Equation (27) yields the fraction of particles which will be trapped by a magnetic mirror. With the inclusion of an applied electric field the trapped fraction has no analytical solution and the equations had to be numerically integrated to compare with the simulation results.

#### 4.2.2. Results

Particles were loaded with a Maxwellian distribution at the center of the magnetic mirror where the magnetic field was minimum. The domain extended from $z = [-0.5, 0.5]$ and particles that reached the edge of the domain were removed. A grid with 100 points was used and a time step of 0.5. The initial number of particles used was $10^4$, the charge $q = -1$, the mass $m = 1$, and the Maxwellian temperature $T = 10^{-4}$. The Boltzmann constant used for seeding particles was set equal to unity. The magnetic field was applied according to the equation $B = 4z^2 + 1$ ($R = 2$) and the potential according to $\phi = Az^2$. The variable $A$ was varied between Case 1 (no electric field), Case 2 (non-confining electric field), and Case 3 (confining electric field) and was set to the values 0, $4 \times 10^{-4}$, and $-4 \times 10^{-4}$ respectively.

Fig. 4 shows the initial and final velocity spaces for all the cases tested. The results qualitatively show that the correct particle trapping behavior was captured. The confining electric field reduced the size of the loss cone while the non-confining field caused the loss cone to grow. A quantitative comparison of the analytical and simulation results for the number of trapped particles is shown in Table 2. Errors were less than one percent, illustrating good agreement between the simulation results and the theory predictions. This test case further verified the implementation of the Q1D Lorentz force in the particle mover. Additional comparisons were made which showed that the Q1D method reproduces the predicted oscillation frequencies of the particles in the magnetic mirror [35].

## 5. Verification with two dimensional simulations

The Q1D method was further verified by comparing with full two-dimensional PIC simulation results. Two-dimensional simulations were performed using XOOPIC (X11-based Object Oriented PIC), a code developed by the University of California,

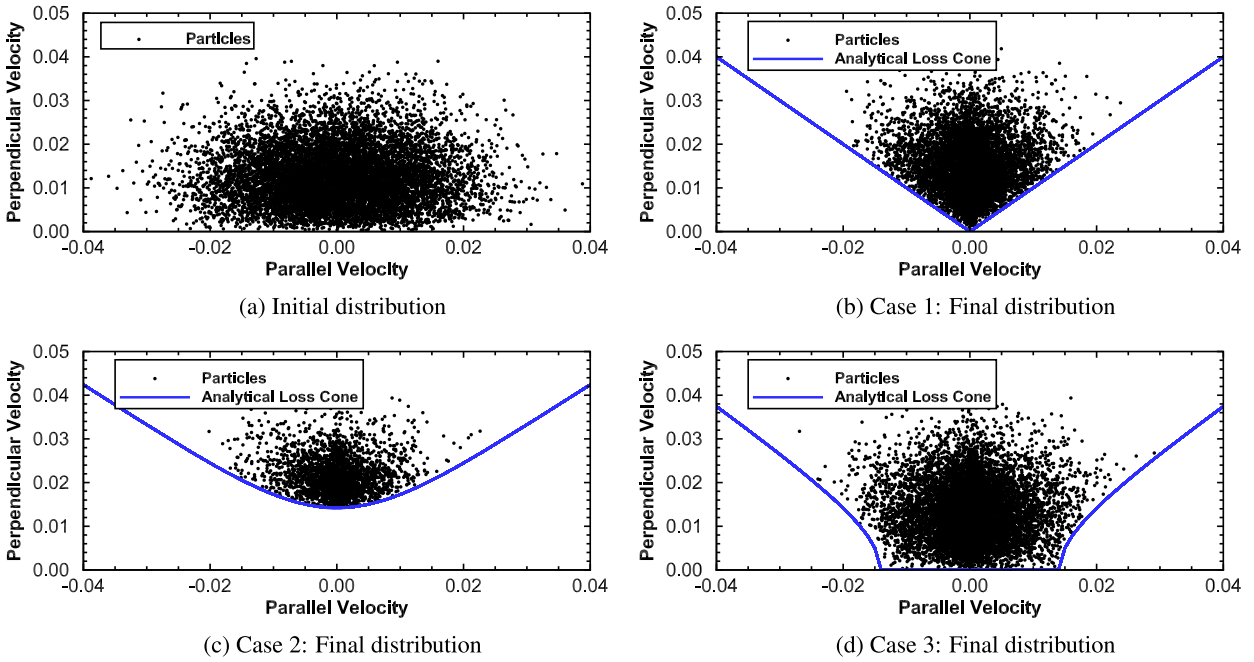


**Fig. 4.** Velocity phase space distributions for magnetic mirror simulations illustrating the capture of the analytical loss cone behavior shown by the line.

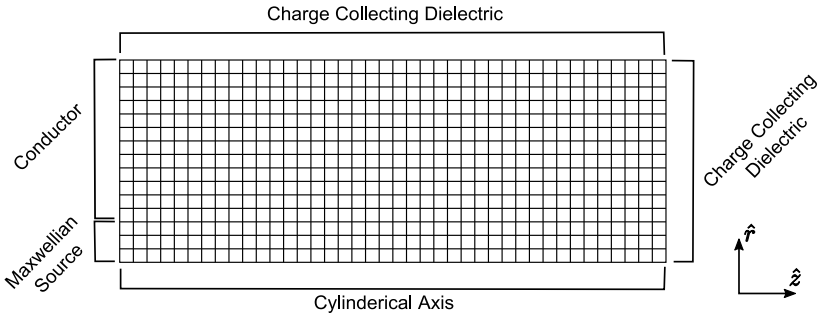


**Fig. 5.** Schematic of grid for XOOPIC simulations of boundary Maxwellian source in a diverging magnetic field. The number of cells has been reduced for clarity.

Berkeley and Michigan State Plasma Theory and Simulation Groups [36]. For the two-dimensional simulations presented herein the electrostatic, cylindrically symmetric solver of XOOPIC was used.

Two test problems were studied. The first of these was a Maxwellian boundary source flowing into a diverging magnetic field with charge collecting boundaries. The second was a volumetric plasma source in a converging–diverging magnetic field. First, two cases for each of the problems will be highlighted to qualitatively compare the Q1D and XOOPIC results. Next, simulations were performed over a broad range of physical parameters (magnetic field strengths, physical dimensions, and plasma properties) and a quantitative comparison made to find the regimes in which the Q1D solution agreed with the 2D solutions.

### *5.1. Boundary Maxwellian source in diverging magnetic field*

The first fully two-dimensional test problem was adapted from the one-dimensional source-collector sheath problem of Schwager [37]. In the 1D Schwager simulations, a Maxwellian ion and electron source was placed at one boundary. The plasma then flows through the domain to a boundary where charge is collected. The original problem was extended to a two-dimensional, cylindrical problem and included a guiding, diverging magnetic field which directs the flow of the Maxwellian source into a two dimensional collector. A schematic of the two dimensional grid used in the XOOPIC simulations is shown in Fig. 5. The grid included five boundary regions: the Maxwellian source, a conductor adjacent to the source, a collector boundary at the radial boundary, a collector boundary at the right boundary, and finally a cylindrical boundary at $r = 0$. Contrary to the Schwager simulations, particles which returned to the Maxwellian source were not re-injected.

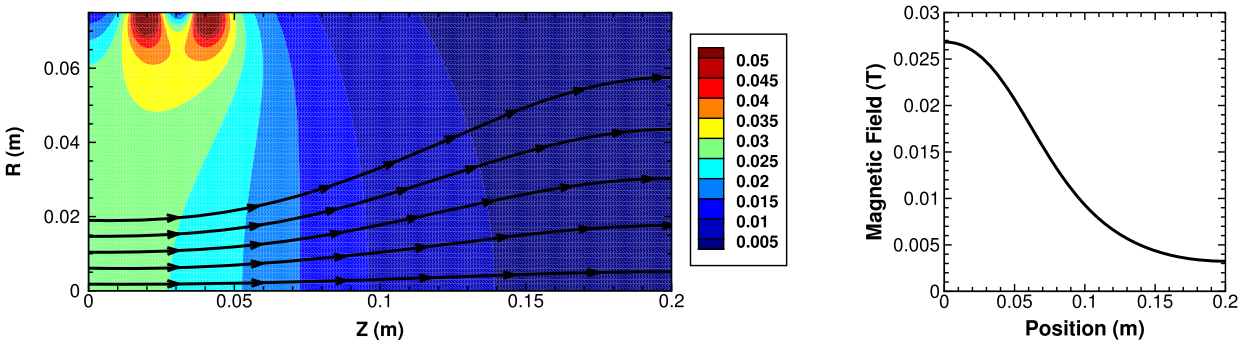


(a) XOOPIC (b) Q1D

**Fig. 6.** Magnetic fields in XOOPIC (left) and Q1D (right) simulations for boundary source in diverging magnetic field. Magnetic field strength (T) contours and streamlines for XOOPIC simulations.

Properties of the Maxwellian source such as the ion density ($n_i$), electron density ($n_e$), ion temperature ($T_i$), electron temperature ($T_e$), and ion mass ($m_i$) were varied between simulations. The magnetic field strength and domain size were also varied. When the domain size was changed the time step was also changed but the total number of cells was kept constant.

Two cases highlight the Q1D effects and the qualitative agreement between the Q1D and 2D simulation results. In these cases the source parameters were: $n_i = n_e = 10^{15}$ m$^{-3}$ and $T_e = 5$ eV. Hydrogen ions were used and only the ion temperature was varied between the two cases with the cold ion (CI) case having an ion temperature $T_i = 300$ K while the hot ion (HI) case has an ion temperature of $T_i = 5$ eV.

The grid consisted of 200 axial and 75 radial cells with a length of 0.2 m and height of 0.075 m. The Maxwellian source was located at $z = 0$ m and extended from $r = [0, 0.015]$ m. The equivalent Q1D grid was 200 cells long with an inlet area set equal to the circular inlet area of the 2D Maxwellian source. The time step used was $\Delta t = 10^{-10}$ s and results are shown at $t = 10^{-5}$ s.

The diverging magnetic field was created by a set of 8 current loops. These loops had radii of 0.075 m and a currents of 1000 A each. The current loops were centered on the cylindrical axis and were positioned at: $-0.04$, $-0.02$, 0.02, 0.04, 0.36, 0.38, 0.42, and 0.44 m. The resulting magnetic field for the 2D and Q1D domains is shown in Fig. 6. These figures illustrate the simplicity of the Q1D model over the fully 2D model.

*5.1.1. Quasi-one-dimensional effects*

First a set of simulations were performed with different variants of the Q1D code to illustrate the effects of the Q1D model on conventional 1D simulations. The variants compared were: one dimensional (1D), area variation effects with no magnetic field force (NBF), area variation with magnetic forces on the electrons but not on the ions (ions demagnetized, IDM), and full Q1D simulations (Full). The IDM case is intended to simulate a problem in which the ions are demagnetized and no longer feel the magnetic field force directly but are still confined to field lines because the electrons are magnetized.

Fig. 7 (left) shows electron density and mean ion velocity profiles for the cold ion simulations. The density profile showed very different behavior between the 1D and full Q1D simulations. The 1D simulation density profiles decreased at the boundaries due to the formation of source and collector sheaths with a nearly constant density through the rest of the domain. Inclusion of Q1D effects resulted in a continued decrease in density due to the plasma expansion along the magnetic field lines. The continued density decrease was captured when the area variation (NBF) was included and was seen in all the Q1D simulations (NBF, IDM, Full).

The ion velocity profiles varied significantly between the Q1D and 1D simulations for the cold ion cases (Fig. 7 (left)). One dimensional results show ion acceleration at the boundary sheaths and no acceleration though the rest of the domain. Inclusion of the varying area (NBF) resulted in a longer acceleration region at the collector boundary. The longer acceleration region was caused by a larger sheath which resulted from the increased Debye length due to lower plasma densities. The IDM and Full simulations showed continued ion acceleration in the diverging magnetic field outside the sheaths due to the incorporation of the magnetic field force effects. Furthermore, both the IDM and Full simulations have the same ion velocity behavior suggesting that direct incorporation of the magnetic field forces on the ions was not necessary for producing ion acceleration in the cold ion simulations.

As discussed previously, the magnetic field forces accelerate particles from strong magnetic field regions to weak magnetic field regions by converting perpendicular kinetic energy to field aligned kinetic energy. In these simulations the hot electrons are rapidly accelerated by the magnetic field force, leaving behind the cold, heavy ions. This results in the formation of an ambipolar electric field which accelerates the ions. The magnetic field forces directly on the ions were unimportant in this test case because the ions are cold. The energy in the ions which could be directed along the axis was small compared to the electron energy and the ambipolar force on the ions was much greater than the magnetic field force directly on the cold ions.

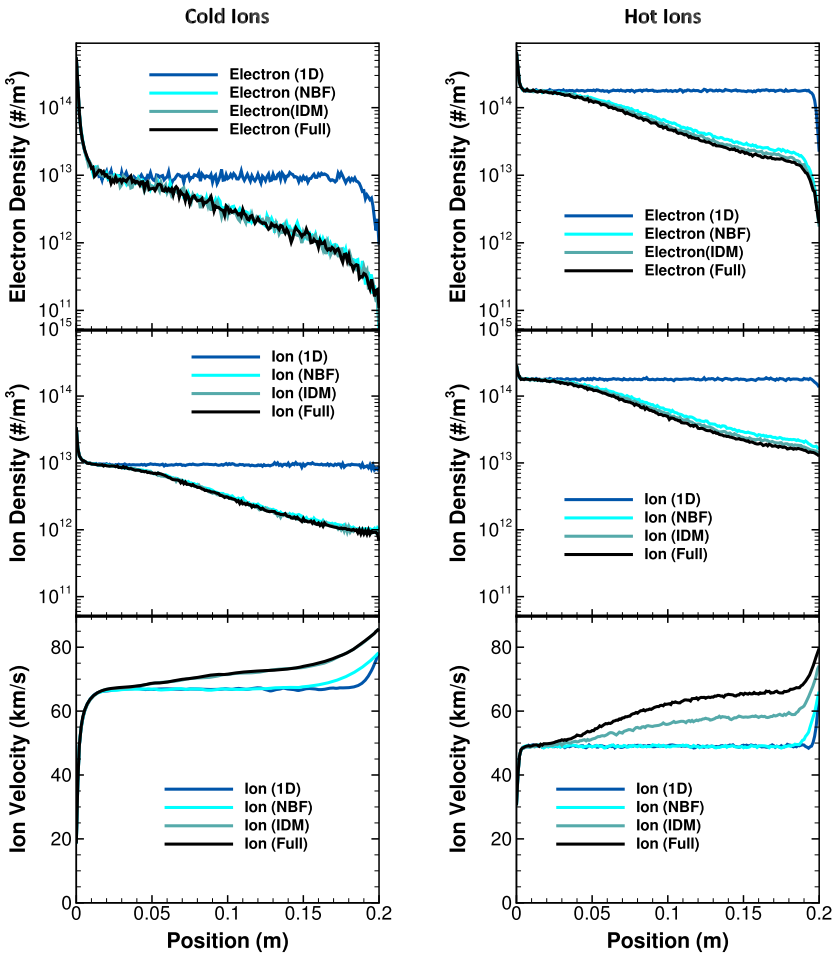


**Fig. 7.** Results from the Maxwellian boundary source simulation with cold ions (left) and hot ions (right) illustrating the effects of the Q1D solver.

The results for the HI case are shown in Fig. 7 (right). The electron density profiles have similar trends to those seen for the CI simulations. The majority of the density decrease was captured by including the effects of the area variation (NBF). However, there were differences in the densities between the NBF, IDM, and Full simulation results as well. These differences are best explained by examining the differences in the mean ion velocity.

Each of the simulation variants for the HI case had a different ion velocity profile. The 1D simulation ion velocity profiles only increase at the boundaries due to the sheaths. The simulations with area variation only (NBF) showed a small extended ion acceleration region due to the longer sheath at the collector boundary. Continued ion acceleration was seen in the demagnetized ion (IDM) simulations due to magnetic field effects on the electrons and the ambipolar electric field. Further acceleration was seen in the Full Q1D simulations once ion magnetic field forces were included. The density differences were caused by these differences in the velocity. At steady state, continuity requires that the density decrease as the ion velocity increases.

Inclusion of the ion magnetic field force in the HI simulations was important because the amount of energy in the ions that could be directed along the axis was the same as the electron energy. In this case the ambipolar force and the magnetic field force directly on the ions were both essential for capturing the ion acceleration.

### *5.1.2. XOOPIC results*

Results from the XOOPIC CI and HI simulations are shown in Figs. 8. Electron density and ion density are shown on contour plots for the entire domain. In the CI simulations the electrons and ions were well confined by the magnetic field. Finite Larmor radius effects are visible in the ion profiles. Electrons were again well confined in the HI simulations. The majority of the ions are still confined in the HI simulation, although there are losses at the plasma edge due to the higher ion energy and therefore higher ion inertia.

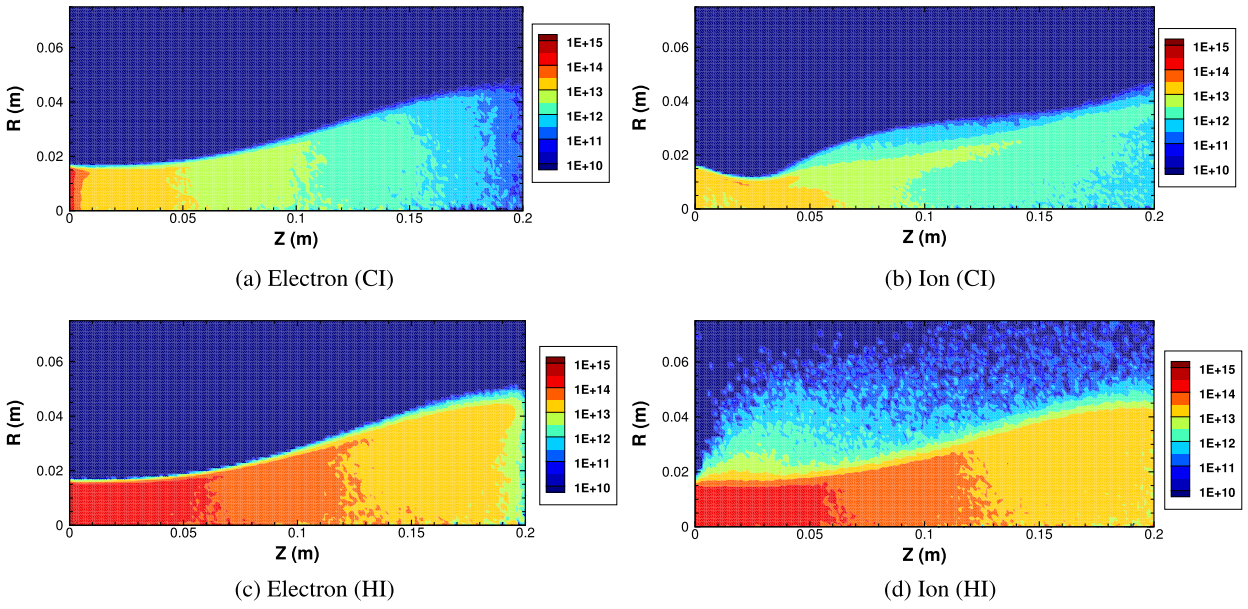


**Fig. 8.** XOOPIC density ($m^{-3}$) contours for Maxwellian boundary source in a diverging magnetic field.

*5.1.3. Comparison of Q1D and XOOPIC results*

Radial averages of plasma properties were taken over the plasma cross-section (defined by the cells which contain the electrons) to compare the 2D and Q1D results. The averaged XOOPIC results are compared to the Q1D results for the CI simulations in Fig. 9 (left). An additional simulation result is shown in which the magnetic field strength in the XOOPIC simulation was increased by a factor of ten (XOOPIC (S)) to illustrate the effects of a stronger magnetic field on the differences between the Q1D and XOOPIC results. Additional Q1D simulations were not performed because the Q1D simulations are independent of magnetic field strength and depend only on magnetic field topology.

Fig. 9 (left) shows that qualitatively the Q1D results agreed well with the fully 2D XOOPIC results for the CI case. Both methods captured the rapid density decreases at the sheaths as well as the continued density decrease in the domain as the plasma expanded along the magnetic field lines. Ion velocity behavior was also similar for both sets of results, capturing sheath effects as well as continued ambipolar acceleration due to the magnetic field directed plasma expansion.

The primary differences between the Q1D and XOOPIC simulation results are the electron density and ion velocities near the source sheaths. After the source sheath, the results approached one another and agree well. This discrepancy was likely due to a combination of 2D effects and the different types of particle moving schemes used by the codes. Specifically, XOOPIC uses an implicit method (Darwin Direct Implicit, DADI) [36] while the Q1D code uses an explicit method [26]. Implicit methods have a tendency to smooth out sharp structures such as sheaths while explicit methods better capture the sudden potential drop. Increasing the magnetic field strength resulted in better agreement between the 2D and Q1D simulations due to better ion confinement. Stronger magnetic fields result in particles that are more magnetized making it more likely that the fundamental assumptions of the Q1D model are met and ultimately result in better agreement.

The HI simulation results are compared in Fig. 9 (right). Overall the density and ion velocity profiles show good qualitative agreement. The Q1D and XOOPIC results for the HI case show closer agreement than the CI cases despite the higher ion inertia in the HI case. Ions with more inertia are less confined by the magnetic field, resulting in more error. The closer agreement resulted primarily from the Q1D code and XOOPIC treating the sheaths more similarly in the HI simulations. In the HI simulations the ion temperature was higher, resulting in a higher ion flux and a lower sheath potential. The lower sheath potential profiles are more similar with the explicit and implicit methods, as expected.

The results from both the CI and HI simulations illustrate that there is good qualitative agreement between the Q1D and XOOPIC results. The density results showed that the Q1D code is capable of capturing the plasma expansion due to the magnetic field. The ion mean velocity results demonstrated that the Q1D code is capable of capturing both direct ion acceleration due to the magnetic field forces as well as acceleration due to ambipolar electric fields produced in the plasma.

These results illustrate that the simplified Q1D model is capable of reproducing fully 2D results when the correct conditions are met. Although XOOPIC was viable for these simulations, scaling to higher densities ($> 10^{17}$ $m^{-3}$) for applications such as electric propulsion is prohibitively expensive computationally for fully 2D simulations [4,38–40,6,41]. The Q1D method alleviates these costs by resolving only one dimension, with far fewer particles needed to perform simulations. The Q1D method only resolves one cell in the radial direction while XOOPIC resolves 75 cells. Therefore, the number of particles required by the Q1D method is 75 times less than those needed by XOOPIC to achieve the similar statistical noise. Fewer particles results in a significant computational cost reduction.

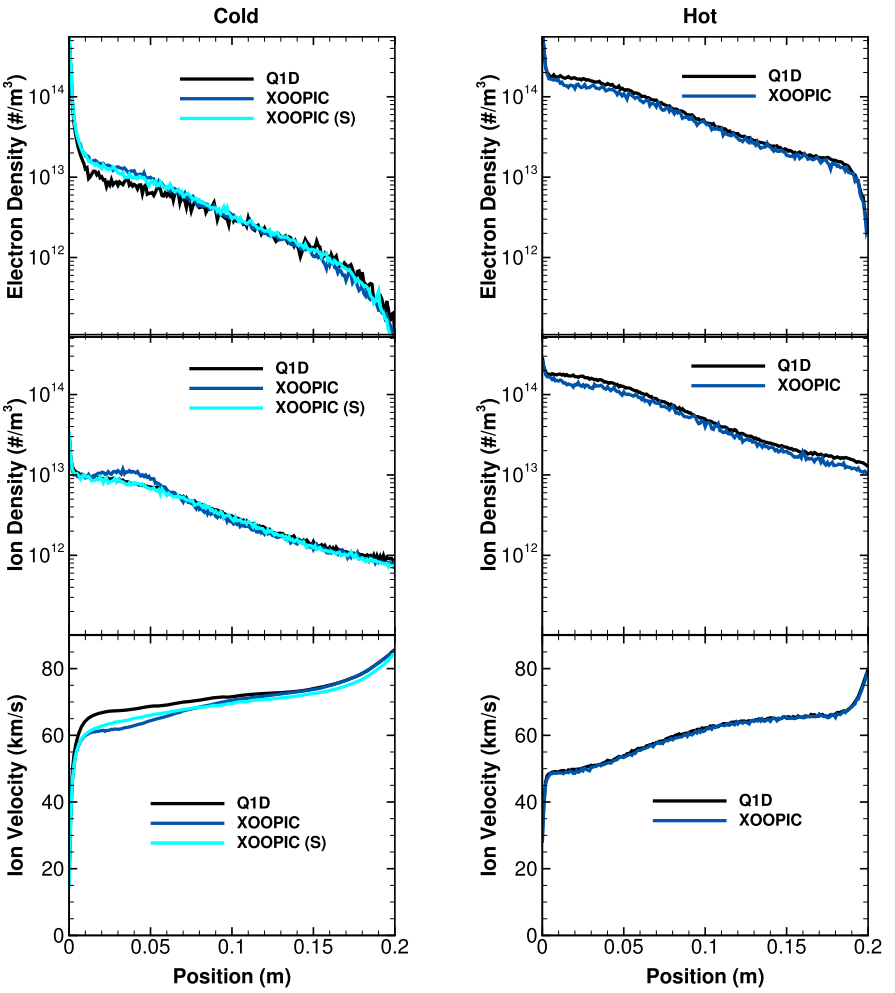


**Fig. 9.** Comparison between XOOPIC and Q1D results of CI (left) and HI (right) simulations for boundary Maxwellian source in a diverging magnetic field.

### 5.2. Particle source in converging–diverging magnetic field

An additional two-dimensional test problem was used to evaluate the ability of the Q1D method to replicate fully 2D simulation results. This problem modeled the flow of a plasma produced by a volumetric source in the center of a magnetic mirror. The properties of the plasma source and magnetic field were again varied to study the regimes in which the Q1D and fully 2D results agree. The varied parameters include the flux rate of particles, the temperatures of the ions and electrons, the mass of the ions, and the magnetic field strength. The physical length of the domain was also varied to test scaling to different problem sizes. Varying these physical properties enabled control of parameters such as the ion and electron Larmor radii which test the validity of the Q1D model.

A schematic of the grid used in the 2D, cylindrical XOOPIC simulations is shown in Fig. 10 to illustrate the location of the boundary conditions. Symmetry boundary conditions were applied at the axis, equipotential conductor boundaries at the left and right boundaries, and exit port boundary conditions at the radial boundary. More details on these boundaries can be found in the XOOPIC documentation [36]. The boundary conditions applied in the Q1D simulations were equipotential boundaries at both boundaries. The inlet cross-sectional area was selected so that the cross-section of the Q1D simulation domain matched the cross-sectional area of the XOOPIC simulation at the center of the domain at the plasma source.

The axial length of the domain ($\hat{z}$) was 0.1 m resolved by 100 cells and the height (for the 2D simulations) was 0.5 m resolved by 50 cells. Particles were seeded at the center of the domain according to a volumetric Maxwellian source spanning $z = [0.049, 0.051]$ m and $r = [0.0, 0.02]$ m. A source rate of $10^{20}$ m$^{-3}$ s$^{-1}$ and electron temperature of $T_e = 5$ eV were used. The only parameter varied in the highlighted cases was the ion temperature which was $T_i = 300$ K for the cold ion case (CI) and $T_i = 5$ eV for the hot ion case (HI). The time step used in these simulation was $\Delta t = 10^{-10}$ s and the results are shown at $t = 10^{-5}$ s.

The magnetic field profile for the XOOPIC simulations is shown in Fig. 11 (left). Magnetic fields were produced by four current loops each with currents of $I = 10^3$ A and radii of 0.025 m. The current loops were centered on the cylindrical axis

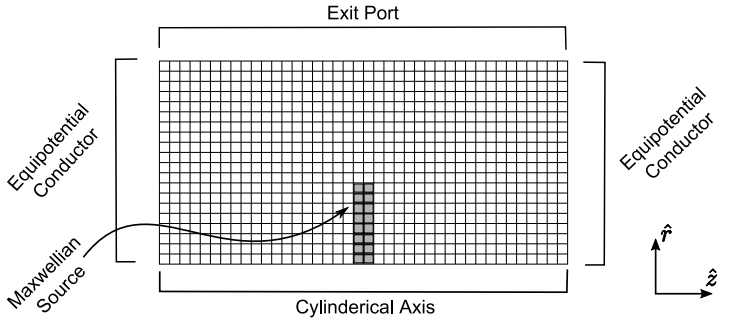


**Fig. 10.** Schematic grid for XOOPIC simulations of a volumetric source in a converging–diverging magnetic field.

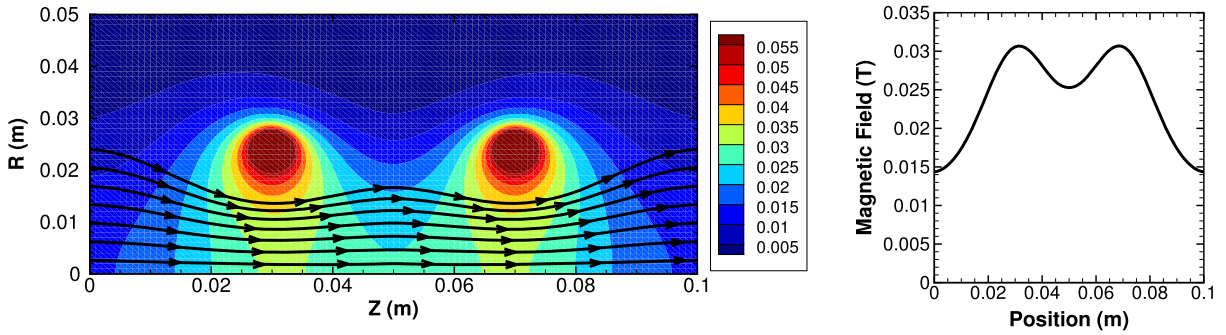


(a) XOOPIC (b) Q1D

**Fig. 11.** Magnetic fields for the XOOPIC and Q1D simulations of a volumetric plasma source in a converging–diverging magnetic field. Contours of magnetic field strength ($T$) and magnetic field lines are shown for XOOPIC simulations.

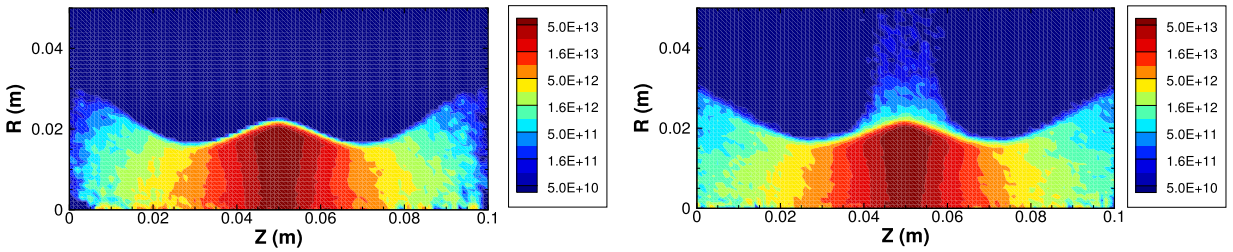


(a) Electron density ($m^{-3}$) (b) Ion density ($m^{-3}$)

**Fig. 12.** XOOPIC results for particle volumetric source simulation with cold ions.

and positioned at: −0.03 m, 0.03 m, 0.07 m, 0.13 m. The equivalent magnetic field in the Q1D model is shown in Fig. 11 (right).

*5.2.1. XOOPIC results*

The XOOPIC results for the CI simulation are shown in Fig. 12. Contours of the electron and ion densities are shown. The electrons were well confined, while the ions had some losses which occur at the center of the domain. Both the ion and electron density were a maximum at the plasma source and then decreased as the plasma flowed through the converging–diverging magnetic field.

Ion losses occurred because the magnetic forces on the ions were not strong enough to completely confine them in the radial direction. This was especially prevalent at the center of the domain, where the magnetic field was monotonically decreasing in the radial direction. The HI simulations showed the same trend as seen in the Maxwellian boundary source simulations with additional ion losses occurring due to the higher ion inertia while the bulk of the ions still remained confined.

*5.2.2. Comparison between Q1D and XOOPIC simulations*

The XOOPIC simulations were compared to the equivalent Q1D simulations by radially averaging over the plasma region. The plasma region was defined as all the cells in which electrons were present. The results for the CI case are compared

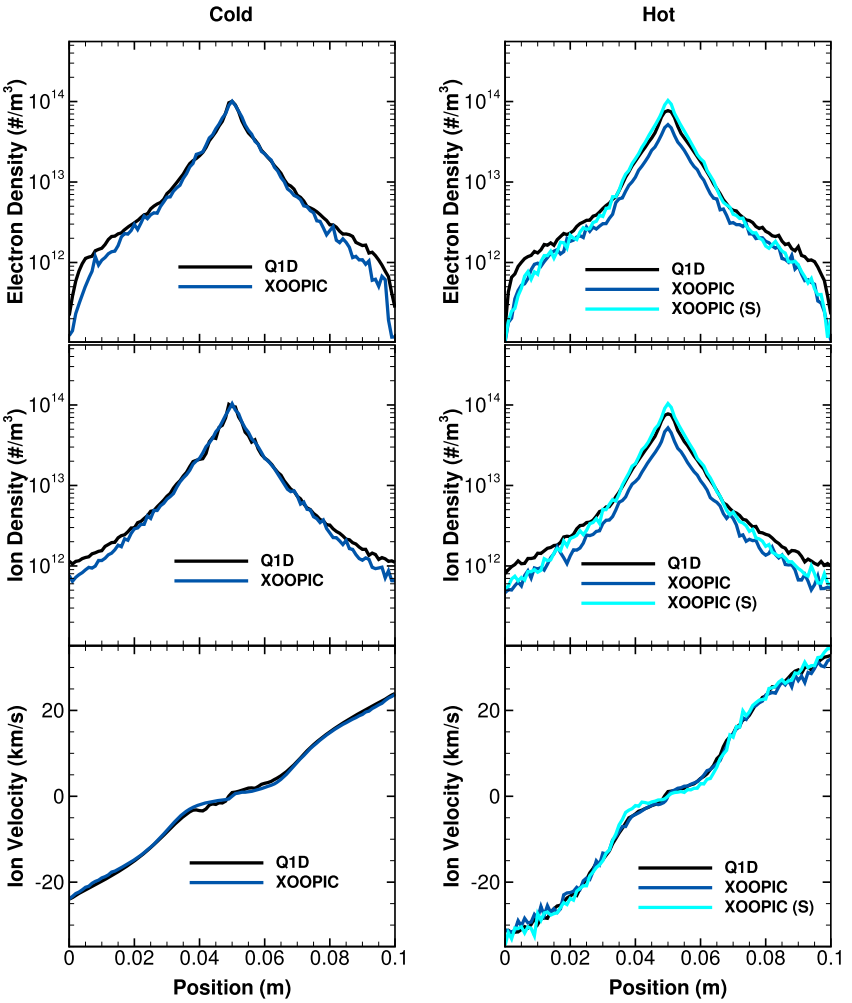


**Fig. 13.** Comparison Q1D and XOOPIC cold ion (left) and hot ion (right) results for volumetric plasma source in a converging–diverging magnetic field.

in Fig. 13 (left). The Q1D and XOOPIC simulations showed a peak in the ion and electron densities at the plasma source and then a decrease as the plasma flows out of the source region. The Q1D results show good agreement with the XOOPIC results near the center of the domain, but start to differ near the boundaries at regions of low density. Some noise was seen in the low density regions, particularly for the XOOPIC simulations, due to the lower number of particles in these regions. An inherent difficulty with the 2D simulation compared to the Q1D simulation is highlighted here: 2D simulations need many more particles to eliminate noise, particularly challenging for a simulation where the density varied by three orders of magnitude. More particles leads to cascade of greater simulation costs and limits the 2D solver to studying low density plasmas. The 2D simulation requires 50 times as many particles (number of radial cells) to achieve statistics and noise similar to the Q1D simulations when all other numerical methods are the same.

The mean ion velocity in the CI simulations shows good agreement throughout the simulation domain. The ion velocity gradually increased in the converging section and then more rapidly increased in the diverging section as the ions were accelerated.

The HI results are shown in Fig. 13 (right). Comparison of the HI Q1D results to XOOPIC results showed greater differences in the density profiles than that seen in the CI case. The Q1D simulations yield the same density profile as XOOPIC but with slightly higher magnitude due to the loss of confinement for some of the high inertia ions in the XOOPIC HI case. Increasing the magnetic field strength by a factor of ten in the XOOPIC simulations (XOOPIC (S)) caused the results to agree more closely in magnitude due to better confinement. Similar to the CI case, the agreement in the converging section was better than the diverging section. Again, this may be due to the lack of particles in the diverging section, particularly for the XOOPIC simulations which were generally more noisy.

The ion axial velocity in the HI simulations showed good agreement. Both the standard and strong XOOPIC simulations had very similar results for the mean ion velocity which agreed well with the Q1D results. The mean ion velocity increased gradually in the converging section, and then rapidly increased in the expansion section.

**Table 3**
Range of parameters for the error analysis parametric study.

| | Boundary source | Volumetric source |
|---|---|---|
| $m_i$ | $2 \times 10^{-27}$–$2 \times 10^{-25}$ kg | $2 \times 10^{-27}$–$7 \times 10^{-26}$ kg |
| $n$ | $10^{15}$–$10^{17}$ m$^{-3}$ | N/A |
| $\Gamma$ | N/A | $10^{20}$ #/(m$^3$ s) |
| $T_e$ | 1–50 eV | 1–50 eV |
| $T_i$ | 0.026–10 eV | 0.026–10 eV |
| $L$ | 0.02–0.2 m | 0.01–0.1 m |
| $B$ | 0.00026–2.6 T | 0.0003–3.0 T |

The simulation results for the volumetric plasma source in a converging–diverging magnetic field gave further proof that the Q1D method is able to reproduce the behavior seen in a fully 2D simulations.

### 5.3. Uncertainty analysis for 2D verification results

A parametric study was performed with a range of plasma parameters for each of the test problems to determine the regimes in which the Q1D results agree with the fully 2D results. The parameters used are summarized in Table 3 and were chosen to evaluate a broad range of plasma length scales (ion and electron Larmor radii, hybrid Larmor radii, etc.) relative to the system dimensions and the size of the domain itself. The densities, temperatures, and domain lengths are parameters relevant to magnetic nozzle physics for electric propulsion.

The combinations of parameters used in the boundary source simulations were selected so that the ratio of the Debye length to the domain length was approximately the same in all simulations. This ratio was maintained by keeping the ratio of the source density to the electron temperature the same for simulations of the same domain length so that the sheath structure would remain relatively small compared to the domain size. When the domain length ($L$) was changed, the ratio also changed to accommodate the change in size.

Quantitative analysis of the errors in the Q1D results compared to the fully 2D results was performed for each of the simulations. The scaling of errors was then evaluated with respect to non-dimensional parameters which characterized each simulation. The Q1D method was derived by assuming that particles are magnetized and follow field lines. Errors should increase as this magnetization assumption becomes less valid by decreasing the magnetic field strength or increasing the particle inertia.

The errors correlated most strongly with the inertial Larmor radius ($r_{L,inertial}$) and the hybrid Larmor radius ($r_{L,H}$).

$$r_{L,inertial} = r_{L,e} + r_{L,i}\frac{v_i}{v_e} \tag{28}$$

$$r_{L,H} = \sqrt{r_{L,e} r_{L,i}} \tag{29}$$

The inertial Larmor radius is a characteristic length derived from treating the ions and electrons as a two-particle system and comparing the inertia of this system with the confining magnetic field force on the electrons. The hybrid Larmor radius is a characteristic length found when analyzing the cross-field, ambipolar drift of a plasma detaching from a magnetic nozzle plasma thruster [42]. These Larmor radii were non-dimensionalized by the gradient magnetic field length scale ($L_B = |B|/|\nabla B| = L_\nabla B_{max}/(B_{max} - B_{min})$) to compare the problem across a range of physical length scales. For the boundary source simulations $L_\nabla$ is equal to the length of the domain and for the volumetric source simulations it is half the length of the domain.

Errors were found by calculating the root-mean-square (RMS) error between the Q1D and fully 2D simulation results. Electron density, ion density, and ion mean velocity RMS errors were compared. The errors were normalized by the maximum value of the parameters in the domain to get a percent error.

#### 5.3.1. Boundary source in a diverging magnetic field

Results for error scaling in the boundary source simulations are shown in Fig. 14. The errors for the densities and ion mean velocity are shown varying with the inertial and hybrid Larmor radii. Density errors are shown for all test cases evaluated, while velocity errors are shown only for a set of test cases with the same electron to ion temperature ratio ($T_e/T_i = 200$). Comparing velocity errors across simulations with different temperature ratios was inconclusive due to the overwhelming importance of the sheath on the ion velocity which scales proportionally to the electron temperature. The differences in the particle movers (explicit and implicit) changed how the source sheath was captured and resulted in significant changes in the ion velocity behavior that overwhelmed any changes that may have been due to the Q1D method.

Both the ion and electron densities showed trends of increasing error as both the inertial and hybrid Larmor radii were increased. Electron density errors were generally lower than the ion density errors due to the better confinement of the electrons. Ion density errors remained below 10% for inertial Larmor radii less than $10^{-2}$ and below 20% for inertial Larmor radii less than $10^{-1}$. Similarly, the error in the ion density stayed approximately below 10% for hybrid Larmor radii less than $3 \times 10^{-2}$. Electron density errors remained below 5% for inertial Larmor radii less than $10^{-2}$ and below 10% for

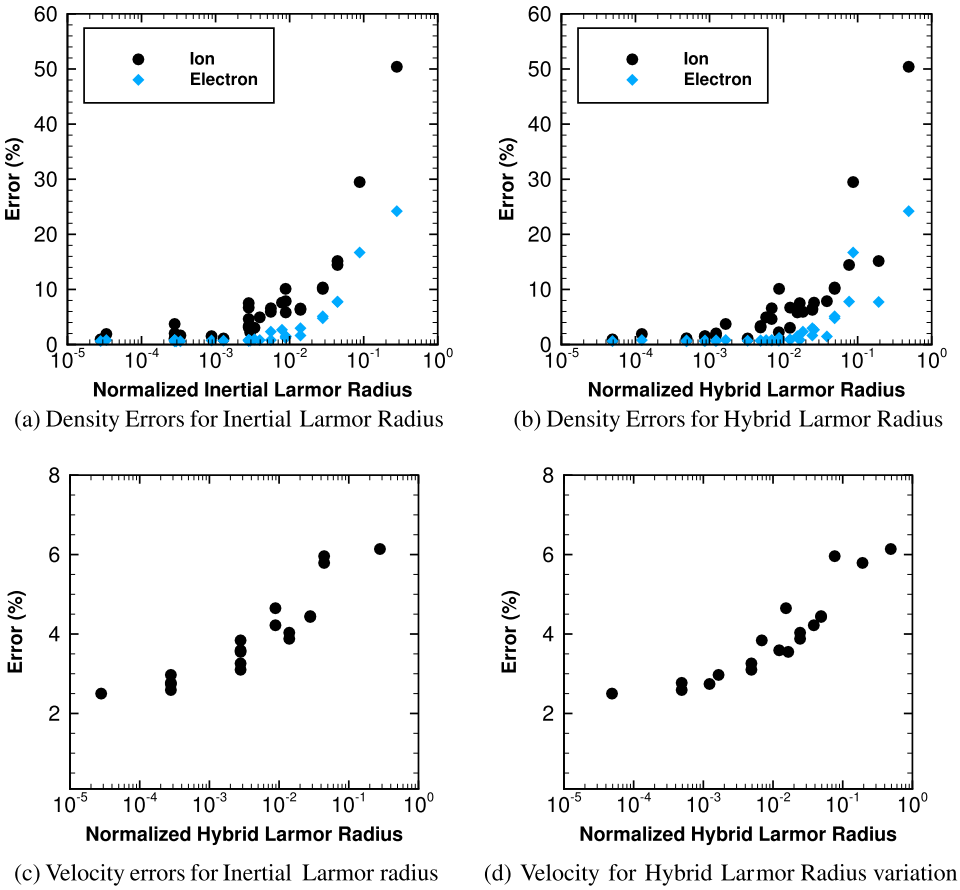


(a) Density Errors for Inertial Larmor Radius (b) Density Errors for Hybrid Larmor Radius

(c) Velocity errors for Inertial Larmor radius (d) Velocity for Hybrid Larmor Radius variation

**Fig. 14.** Scaling of errors for boundary source in a diverging magnetic field. All radii are normalized by the magnetic field length scale.

inertial Larmor radii less than $10^{-1}$. Similarly, the electron density error stayed approximately below 5% for inertial Larmor radii less than $3 \times 10^{-2}$.

Ion velocity errors showed a general trend of increasing error as both the inertial and hybrid Larmor radii were increased. The ion velocity errors remained low ($<7\%$) because the source sheath was the dominating feature affecting the ion velocity and by design the source sheath structure was kept the same between simulations. Furthermore, changing the magnetic field did not greatly affect the sheath structure near the source because the magnetic field is mostly parallel to the sheath direction.

Based on these results it is recommended that the non-dimensionalized inertial and hybrid Langmuir radii should be less than 0.1 for the Q1D method to capture 2D physics in magnetic field guided plasma expansions.

*5.3.2. Particle source in a converging–diverging field*

Error analysis results for the volumetric particle source in a converging–diverging magnetic field are shown in Fig. 15. Trends of increasing error are shown as both the inertial and hybrid Larmor radii increased. In these simulations the ion and electron densities scaled with one another, contrary to the boundary source in the diverging field where the ions showed a larger error. The reason for this difference may be that there is no sheath present in these simulations which in the boundary source case accelerates the ions as they enter the bulk. High ion velocities imply that the particles have more inertia, which makes them more difficult to confine and results in larger errors. For the volumetric plasma source simulations there was no sheath, resulting in the ions maintaining a low velocity until they were accelerated due to the ambipolar and magnetic field forces.

Ion and electron density errors of less than 10% were achieved for $r_{L,inertial} \leq 2 \times 10^{-3}$ while errors less than 20% required $r_{L,inertial} \leq 10^{-2}$. Similarly, errors of less than 10% were found for $r_{L_H} \leq 7 \times 10^{-3}$ while errors less than 20% were obtained for $r_{L_H} \leq 2 \times 10^{-2}$. Errors begin to rapidly increase after 20% for both inertial and hybrid Larmor radii.

## 6. Discussion

The simulations performed in this paper and the error analysis yielded two key results: the Q1D model reproduced two-dimensional results when the plasma is well confined to the magnetic field and the errors between the Q1D model and

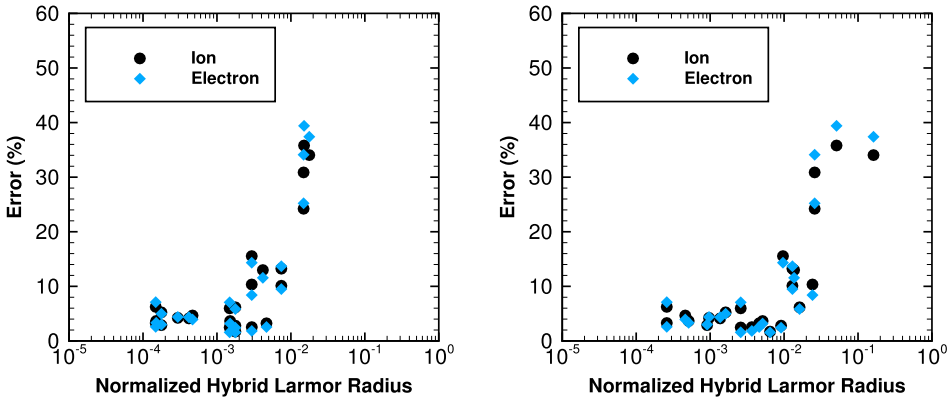


(a) Density Errors for Inertial Larmor Radius (b) Density Errors for Inertial Larmor Radius

**Fig. 15.** Scaling of errors for particle source in a converging–diverging magnetic field simulations.

the 2D results scale with intuitive parameters based on the non-dimensional inertial and hybrid Larmor radii. These results demonstrate that the Q1D model is a good approximation for the 2D plasma physics in the relevant regimes and that errors scale consistently.

Collisions must also be considered when evaluating the validity of the Q1D method for replicating 2D results. The assumption of magnetization and confinement to field lines may no longer be valid if particles are colliding frequently with particles or walls. Regimes which include frequent collisions do not preclude the use of the Q1D model, but require further analysis, verification, and testing of the Q1D method.

The Q1D method was developed to enable the simulation of high density, magnetic field guided plasma flows by reducing the computational cost compared to fully 2D simulations while still capturing the relevant physics. PIC computational costs typically scale as $O(N_p + N_c log(N_c))$ where $N_p$ is the number of particles used and $N_c$ is the number of cells [43,44]. The number of particles required is based on stability requirements and can be assumed to be proportional to the number of cells by a proportionality constant $\alpha$ so that $N_p = \alpha N_c$ implying $O(\alpha N_c + N_c log(N_c))$. Two dimensional simulations require more cells than 1D simulations by virtue of resolving the second dimension. For large $\alpha$ the computational cost for 2D simulations increases approximately by a factor equal to the number of cells resolved in the second direction. The Q1D method removes this cost increase and the overall cost should be comparable to a one-dimensional code which includes the Boris magnetic field push because the Q1D algorithms have effectively replaced this step.

## 7. Conclusion

A novel kinetic method for the quasi-one-dimensional simulation of magnetic field guided plasma dynamics was developed. The Q1D method reduces the plasma physics by assuming that the plasma is confined to a magnetic flux tube with constant properties over the plasma cross-section. The simplification of the problem significantly reduced the computational cost while capturing much of the important physics.

The Q1D method was implemented into an existing 1D PIC code by the inclusion of cross-sectional areas dependent on the magnetic field strength and simplified magnetic field forces. Verification was performed with test cases of two particle motion and magnetic mirror machines. The Q1D model was further verified by comparing with fully two-dimensional simulations of magnetic field guided boundary and volumetric sources using XOOPIC. The Q1D model reproduced the fully 2D results in the appropriate regimes defined by the non-dimensional inertial and hybrid Larmor radii. Errors between the Q1D and 2D results scaled with the inertial and hybrid Larmor radii.

In short, the Q1D model was shown to be enabling for the simulation of two-dimensional effects in a magnetic field guided plasma without the inherent computational costs of a fully 2D system. This work has verified the utility of this model and has outlined the process for incorporating the method in a 1D PIC code.

## Acknowledgements

Funding: This work was supported by a NASA Space Technology Research Fellowship under grant NNX13AO19H. This research was also supported by DARPA contract number NNA15BA42C, University of Michigan Rackham Graduate School grants, and the Michigan Institute of Plasma Science and Engineering graduate fellowship. Simulations were performed on the NASA Pleiades Supercomputer (Grant NNX13AO19H) and the University of Michigan Advanced Research Computing Flux Cluster. This work also used the Extreme Science and Engineering Discovery Environment (XSEDE), which is supported by National Science Foundation grant number ACI-1053575.

Thank you to Alexander G.R. Thomas, Iain D. Boyd, and Kentaro Hara for insights provided in this research.

## References


[1] T.E. Cravens, Physics of Solar System Plasmas, Cambridge University Press, 2004.
[2] S. Robertson, A reduced set of gyrofluid equations for plasma flow in a diverging magnetic field, Phys. Plasmas 23 (4) (2016) 043513, http://dx.doi.org/10.1063/1.4947560 (1994-present).
[3] S.M. Gorbatkin, L.A. Berry, J.B. Roberto, Behavior of Ar plasmas formed in a mirror field electron cyclotron resonance microwave ion source, J. Vac. Sci. Technol., A 8 (3) (1990) 2893–2899, http://dx.doi.org/10.1116/1.576645.
[4] C. Charles, Plasmas for spacecraft propulsion, J. Phys. D, Appl. Phys. 42 (16) (2009) 163001.
[5] F. Ebersohn, S. Sharath, D. Staack, J. Shebalin, B. Longmier, C. Olsen, Magnetic nozzle plasma plume: review of crucial physical phenomena, in: AIAA-2012-4274, 47th AIAA/ASME/SAE/ASEE Joint Propulsion Conference, Atlanta, GA, 2012.
[6] J. Little, A. Rubin, E. Choueiri, Similarity parameter evolution within a magnetic nozzle with applications to laboratory plasmas, in: IEPC-2011-229, 30th International Electric Propulsion Conference, Wiesbaden, Germany, 2011.
[7] K. Takahashi, Y. Itoh, T. Fujiwara, Operation of a permanent-magnets-expanding plasma source connected to a large-volume diffusion chamber, J. Phys. D, Appl. Phys. 44 (1) (2010) 015204.
[8] O.A. Popov, Characteristics of electron cyclotron resonance plasma sources, J. Vac. Sci. Technol., A 7 (3) (1989) 894–898, http://dx.doi.org/10.1116/1.575816.
[9] O.A. Popov, High Density Plasma Sources: Design, Physics and Performance, Elsevier, 1996.
[10] J. Asmussen, Electron cyclotron resonance microwave discharges for etching and thin-film deposition, J. Vac. Sci. Technol., A 7 (3) (1989) 883–893.
[11] G. Guan, M.E. Mauel, W.M. Holber, J.B.O. Caughman, A fluid description for the discharge equilibrium of a divergent electron cyclotron resonance plasma source, Phys. Fluids, B Plasma Phys. 4 (12) (1992) 4177–4186, http://dx.doi.org/10.1063/1.860324 (1989–1993).
[12] M. Matsuoka, K. Ono, Magnetic field gradient effects on ion energy for electron cyclotron resonance microwave plasma stream, J. Vac. Sci. Technol., A 6 (1) (1988) 25–29, http://dx.doi.org/10.1116/1.574990.
[13] S. Andersen, V. Jensen, P. Nielsen, N. D'Angelo, Continuous supersonic plasma wind tunnel, Phys. Fluids 12 (3) (1969) 557–560.
[14] C. Charles, Plasmas for spacecraft propulsion, J. Phys. D, Appl. Phys. 42 (16) (2009) 163001, http://dx.doi.org/10.1088/0022-3727/42/16/163001.
[15] B.W. Longmier, E.A.B. Iii, M.D. Carter, L.D. Cassady, W.J. Chancery, F.R.C. Díaz, T.W. Glover, N. Hershkowitz, A.V. Ilin, G.E. McCaskill, C.S. Olsen, J.P. Squire, Ambipolar ion acceleration in an expanding magnetic nozzle, Plasma Sources Sci. Technol. 20 (1) (2011) 015007.
[16] R. Gerwin, Integrity of the plasma magnetic nozzle, Tech. Rep. NASA/TP-2009-213439, NASA Technical Reports Server, 2009.
[17] T.I. Gombosi, C.E. Rasmussen, Transport of gyration-dominated space plasmas of thermal origin: 1. Generalized transport equations, J. Geophys. Res. Space Phys. 96 (A5) (1991) 7759–7778.
[18] E. Ahedo, M. Merino, Two-dimensional supersonic plasma acceleration in a magnetic nozzle, Phys. Plasmas 17 (2010) 073501.
[19] R. Winglee, T. Ziemba, L. Giersch, J. Prager, J. Carscadden, B. Roberson, Simulation and laboratory validation of magnetic nozzle effects for the high power helicon thruster, Phys. Plasmas 14 (2007) 063501.
[20] J.M. Stone, T.A. Gardiner, P. Teuben, J.F. Hawley, J.B. Simon, Athena: a new code for astrophysical mhd, Astrophys. J. Suppl. Ser. 178 (1) (2008) 137.
[21] H. Lorzel, P. Mikellides, Three-dimensional modeling of magnetic nozzle processes, AIAA J. 48 (7) (2010) 1494–1503.
[22] J. Denavit, Collisionless plasma expansion into a vacuum, Phys. Fluids 22 (7) (1979) 1384–1392 (1958–1988).
[23] A. Meige, R. Boswell, C. Charles, J.-P. Boeuf, G. Hagelaar, M. Turner, One-dimensional simulation of an ion beam generated by a current-free double-layer, IEEE Trans. Plasma Sci. 33 (2) (2005) 334–335, http://dx.doi.org/10.1109/TPS.2005.844956.
[24] S. Rao, N. Singh, Numerical simulation of current-free double layers created in a helicon plasma device, Phys. Plasmas 19 (9) (2012) 093507, http://dx.doi.org/10.1063/1.4754598.
[25] N. Singh, S. Rao, P. Ranganath, Waves generated in the plasma plume of helicon magnetic nozzle, Phys. Plasmas 20 (3) (2013) 032111, http://dx.doi.org/10.1063/1.4795734 (1994-present).
[26] C. Birdsall, Particle-in-cell charged-particle simulations, plus Monte Carlo collisions with neutral atoms, PIC-MCC, IEEE Trans. Plasma Sci. 19 (2) (1991) 65–85, http://dx.doi.org/10.1109/27.106800.
[27] C. Birdsall, A. Langdon, Plasma Physics via Computer Simulation, CRC Press, 2004.
[28] J. Verboncoeur, Particle simulation of plasmas: review and advances, Plasma Phys. Control. Fusion 47 (5A) (2005) A231.
[29] J. Vedin, K. Rönnmark, Particle-fluid simulation of the auroral current circuit, J. Geophys. Res. Space Phys. 111 (A12) (2006).
[30] H. Vu, J. Brackbill, Accurate numerical solution of charged particle motion in a magnetic field, J. Comput. Phys. 116 (2) (1995) 384–387.
[31] F. Chen, Introduction to Plasma Physics and Controlled Fusion, vol. 1, Plenum Press, New York, 1984.
[32] R. Comfort, The magnetic mirror force in plasma fluid models, in: Modeling Magnetospheric Plasma, American Geophysical Union, 1988, pp. 51–53.
[33] J. Boris, Relativistic plasma simulation–optimization of a hybrid code, in: Proc. Fourth Conf. Num. Sim. Plasmas, Naval Res. Lab., Wash. DC, 1970, pp. 3–67.
[34] K.L. Cartwright, J.P. Verboncoeur, C.K. Birdsall, Loading and injection of Maxwellian distributions in particle simulations, J. Comput. Phys. 162 (2) (2000) 483–513.
[35] F. Ebersohn, J. Sheehan, B. Longmier, J. Shebalin, Quasi-one-dimensional code for particle-in-cell simulation of magnetic nozzle expansion, in: AIAA-2014-4027, 50th AIAA/ASME/SAE/ASEE Joint Propulsion Conference, Cleveland, OH, 2014.
[36] J. Verboncoeur, A. Langdon, N. Gladd, An object-oriented electromagnetic PIC code, Comput. Phys. Commun. 87 (1) (1995) 199–211.
[37] L. Schwager, C. Birdsall, Collector and source sheaths of a finite ion temperature plasma, Phys. Fluids, B Plasma Phys. 2 (5) (1990) 1057–1068.
[38] F. Ebersohn, Gas Kinetic Study of Magnetic Field Effects on Plasma Plumes, MS thesis, Texas A&M University, 2012.
[39] F. Chang-Diaz, The VASIMR rocket, Sci. Am. 283 (5) (2000) 90–97.
[40] K. Takahashi, T. Lafleur, C. Charles, P. Alexander, R. Boswell, Electron diamagnetic effect on axial force in an expanding plasma: experiments and theory, Phys. Rev. Lett. 107 (23) (2011) 235001.
[41] J. Sheehan, T. Collard, B. Longmier, I. Goglio, New low-power plasma thruster for nanosatellites, in: AIAA-2014-3914, 50th AIAA/ASME/SAE/ASEE Joint Propulsion Conference, 2014.
[42] E. Hooper, Plasma detachment from a magnetic nozzle, J. Propuls. Power 9 (5) (1993) 757–763.
[43] R.W. Hockney, J.W. Eastwood, Computer Simulation Using Particles, CRC Press, 1988.
[44] L. Greengard, V. Rokhlin, A fast algorithm for particle simulations, J. Comput. Phys. 73 (2) (1987) 325–348.